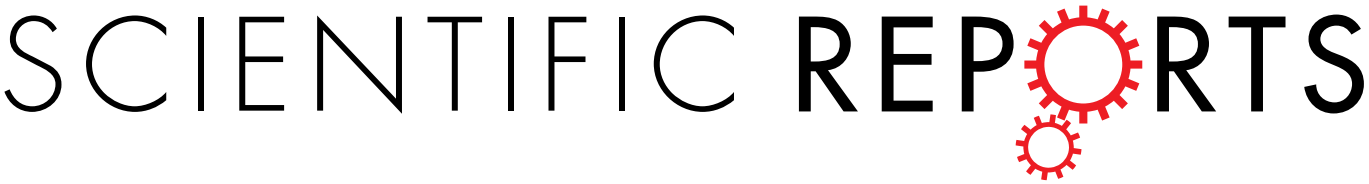

OPEN

Received: 30 December 2015
Accepted: 13 May 2016
Published: 03 June 2016

An autism-associated mutation in $Ca_V1.3$ channels has opposing effects on voltage- and Ca^{2+}-dependent regulation

Worawan B. Limpitikul, Ivy E. Dick, Manu Ben-Johny & David T. Yue†

$Ca_V1.3$ channels are a major class of L-type Ca^{2+} channels which contribute to the rhythmicity of the heart and brain. In the brain, these channels are vital for excitation-transcription coupling, synaptic plasticity, and neuronal firing. Moreover, disruption of $Ca_V1.3$ function has been associated with several neurological disorders. Here, we focus on the *de novo* missense mutation A760G which has been linked to autism spectrum disorder (ASD). To explore the role of this mutation in ASD pathogenesis, we examined the effects of A760G on $Ca_V1.3$ channel gating and regulation. Introduction of the mutation severely diminished the Ca^{2+}-dependent inactivation (CDI) of $Ca_V1.3$ channels, an important feedback system required for Ca^{2+} homeostasis. This reduction in CDI was observed in two major channel splice variants, though to different extents. Using an allosteric model of channel gating, we found that the underlying mechanism of CDI reduction is likely due to enhanced channel opening within the Ca^{2+}-inactivated mode. Remarkably, the A760G mutation also caused an opposite increase in voltage-dependent inactivation (VDI), resulting in a multifaceted mechanism underlying ASD. When combined, these regulatory deficits appear to increase the intracellular Ca^{2+} concentration, thus potentially disrupting neuronal development and synapse formation, ultimately leading to ASD.

L-type voltage-gated Ca^{2+} channels are critical conduits for Ca^{2+} entry into many excitable cells. The $Ca_V1.3$ channel represents a distinctive subtype of these channels, important in neurological[1–4], cardiac[3–5], and endocrine[4,6,7] function. The biophysical properties of these channels are thus precisely tuned to this function, as they are activated at relatively hyperpolarized potentials compared to other L-type voltage-gated Ca^{2+} channels[3,8–12] and undergo distinct forms of negative feedback regulation[3,13,14].

$Ca_V1.3$ channels employ two major forms of feedback regulation, voltage-dependent inactivation (VDI) and Ca^{2+}-dependent inactivation (CDI)[14]. These two regulatory processes are controlled within each cell type, utilizing splice variation[3,15–17], RNA editing[18,19], and auxiliary subunit pairing[20,21] to tune the inactivation properties of the channel to specific cellular functions. In particular, both splice variation and RNA editing are able to modulate both CDI[3,10,17–19,22–24] and channel open probability[15] by tailoring the components contained within the channel carboxy tail. In addition, channel beta subunits are known to both traffic channels to the membrane[25,26] and alter their voltage inactivation properties[21,26–28].

The precise control of these regulatory processes are a vital component of normal physiology and disruption of this regulation has been linked to multiple human disorders including autism[3,29–31], auditory deficits[32,33], and hyperaldosteronism[34,35]. In mice, knockout of $Ca_V1.3$ results in profound deafness and severe bradycardia[33,36], while in humans a similar phenotype is observed in patients harboring a 3-base pair insertion in exon 8b[32]. This insertion abolishes channel conduction, resulting in sinoatrial node dysfunction and deafness (SANDD) syndrome, a phenotype similar to that described in $Ca_V1.3$-knockout mice. Moreover, multiple gain-of-function mutations have been linked to patients with hyperaldosteronism[34,35]. Finally, two gain-of-function mutations in $Ca_V1.3$ (G407R and A749G) have been linked to autism spectrum disorders (ASD)[30,31,37]. Prior studies of these two mutations demonstrated alterations in channel gating including a hyperpolarizing shift in channel activation

Calcium Signals Laboratory, Departments of Biomedical Engineering and Neuroscience, The Johns Hopkins University School of Medicine, Ross Building, Room 713,720 Rutland Avenue, Baltimore, MD 21205, USA. †Deceased. Correspondence and requests for materials should be addressed to W.B.L. (email: wlimpit1@jhmi.edu) or I.E.D. (email: ied@jhu.edu)

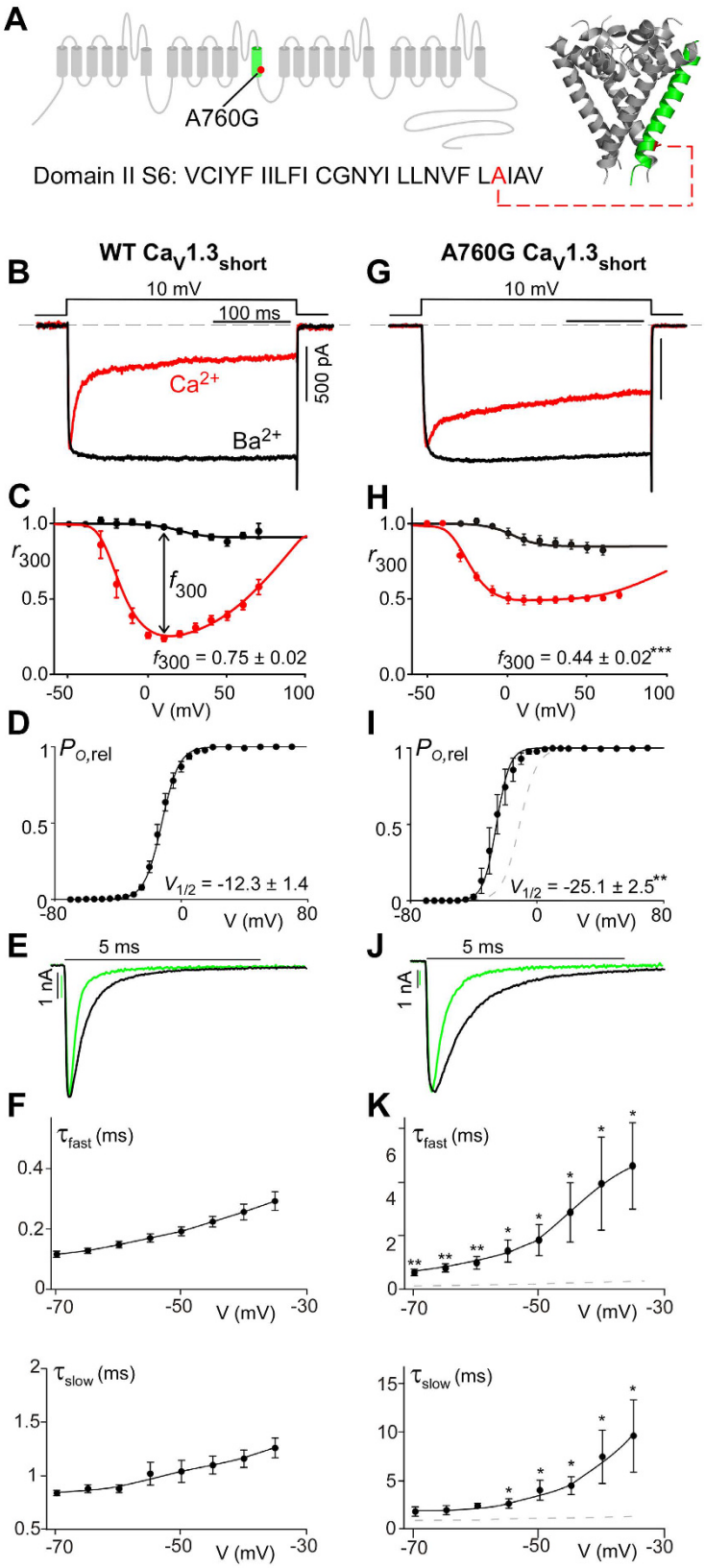

Figure 1. A760G decreases CDI and promotes channel activation. (**A**) Cartoon representing $Ca_v1.3$ and the location of the autism-associated mutation A760G. Left, the A760G missense mutation resides in the S6 helix of domain II. Right, structural homology model of $Ca_v1.3$ S5/S6 segments, based on Na_VAb with the A760G highlighted in red. (**B**) Exemplar Ca^{2+} (red) and Ba^{2+} (black) current traces through WT $Ca_V1.3_{short}$ evoked by a 10-mV depolarizing step. Currents are normalized for comparison. Scale bar corresponds to the Ca^{2+} trace. (**C**) Population data of fraction of current remaining after 300 ms (r_{300}) for Ca^{2+} (red) and Ba^{2+} (black). f_{300}

determined at 10 mV (n = 12). Data are plotted as mean ± SEM here and throughout. (**D**) The activation curve for WT $Ca_V1.3_{short}$ obtained via a tail activation protocol with Ba^{2+} as the charge carrier (n = 6). (**E**) Exemplar Ba^{2+} tail currents obtained from a transition from 80 mV to −40 mV (black) and −60 mV (green). Traces are normalized to one another. Scale bars correspond to the traces of the same color. (**F**) Population data of the fast (top) and slow (bottom) deactivation time constants (τ) plotted as a function of voltage (n = 5). (**G**) Exemplar Ca^{2+} (red) and Ba^{2+} (black) current traces through A760G $Ca_V1.3_{short}$ evoked by a 10-mV depolarizing step. Compared to that of WT (**B**), Ca^{2+} current through A760G channels display significantly less CDI. (**H**) Population data of r_{300} for Ca^{2+} (red) and Ba^{2+} (black) currents through A760G channels. CDI is significantly smaller (***$p < 0.001$, n = 6) than that of the WT channels. (**I**) The activation curve of A760G $Ca_V1.3_{short}$ channels (black) shows a 13-mV hyperpolarizing shift (**$p < 0.01$, n = 4) compared to WT (reproduced in gray). (**J**) Exemplar Ba^{2+} tail currents for the A760G channel, obtained from a transition from 80 mV to −40 mV (black) and −60 mV (green). (**K**) Population data of the fast (top) and slow (bottom) deactivation time constants (τ) plotted as a function of voltage for the A760G channel. Deactivation is significantly slowed as compared to WT reproduced as the gray dashed line (*$p < 0.05$, **$p < 0.01$, n = 4).

and inactivation curves[31], but the differential effects on CDI versus VDI have yet to be determined. Discerning these precise effects may be highly relevant to understanding the mechanism of pathogenesis, as disruption of each of these components in the related $Ca_V1.2$ L-type channel has been shown to underlie Timothy syndrome (a severe multisystem disorder including autism and cardiac deficits)[38–40], as well as long-QT syndrome associated with mutations in calmodulin[41]. It is interesting to note that, unlike the $Ca_V1.2$ channelopathies, $Ca_V1.3$ mutations have often been associated with single-system phenotypes[30,37], despite the multi-system distribution of $Ca_V1.3$ channels. This isolation of symptoms is curious and requires further mechanistic investigation.

Here, we examine the underlying channel regulatory deficits of the autism-associated A760G mutation in rat $Ca_V1.3$ (equivalent to the A749G[31] or A769G[30] mutation in the human, depending on the channel backbone), focusing on the specific biophysical alterations produced by the mutation. We find that the mutation causes a significant reduction of CDI and a delay in channel deactivation in two major channel splice variants. In addition, we utilize an allosteric model of channel gating to gain insight into the underlying mechanism of this CDI deficit. Further examination of the biophysical defects of this mutation also revealed a beta subunit-dependent increase in VDI, an effect which would oppose the Ca^{2+} overload due to the decrease in CDI and a delay in channel deactivation. Thus the severe effects of this 'gain-of-function' mutation could be mitigated by a 'loss-of-function' effect on VDI.

Results

A760G significantly decreases CDI and alters $Ca_V1.3$ channel gating. Voltage-gated Ca^{2+} channel α1-subunits are composed of four domains, each containing six transmembrane α -helices (Fig. 1A). The four S6 helices line the channel pore through which Ca^{2+} enters the cell. The intracellular portion of these S6 helices form the activation gate of the channel, and mutations within this region are known to alter channel activation[31,42–46]. Moreover, the S6 helices are known to contribute to VDI and CDI in many Ca_V channels, including $Ca_V1.3$[14,40,42–50]. Thus, the effect of the A760G mutation on channel activation and inactivation[31] may be explained by its location in the S6 helix of domain II (IIS6).

In order to study the effects of the A760G mutation on Ca^{2+} regulation of channels, we undertook whole-cell voltage clamp recordings of $Ca_V1.3$ channels heterologously expressed in HEK293 cells. To minimize the possible confounding effects on CDI measurements, the channels were co-expressed with the β_{2a} subunit which is known to minimize VDI[21,26,28,51,52]. In addition, an internal solution containing 10 mM BAPTA was utilized to restrict Ca^{2+} elevation to only the nanodomain of the channel, thus diminishing cell-to-cell variability[53,54]. Figure 1B shows exemplar current traces for wild-type (WT) $Ca_V1.3$. The sharp decay of Ca^{2+} current (red) evoked by a 10-mV depolarizing step depicts CDI, while the Ba^{2+} current trace (black) exhibits only VDI, which is mostly absent here due to the choice of β subunit. This robust CDI can be observed in the population data, where the fraction of current remaining after 300-ms depolarization (r_{300}) is displayed as a function of voltage (Fig. 1C), and the U-shaped dependence on voltage recapitulates a classic hallmark of CDI[55,56]. Here, the difference between the r_{300} values for Ca^{2+} and Ba^{2+}, normalized by the Ba^{2+} r_{300}, gauges the magnitude of CDI (f_{300}). However, when the A760G mutation is introduced into these channels, a drastic reduction in the speed and magnitude of CDI is observed (Fig. 1G, Supplementary Figure 1). This effect is further evident in the population data across multiple voltages (Fig. 1H) illustrating a clear CDI deficit due to the autism-associated A760G mutation.

Beyond CDI, S6 mutations are likely to affect channel activation[31,42–46]. We therefore probed the effect of the A760G on the voltage dependence of $Ca_V1.3$ channel activation. Here, we measured the relative open probability ($P_{o,rel}$) of the channels across voltages via a tail activation protocol optimized for $Ca_V1.3$ channels[54] (Fig. 1D). Introduction of the A760G mutation produced a significant hyperpolarizing shift (13 mV; $p < 0.01$) in channel activation (Fig. 1I), consistent with previous studies of this channel[31]. Moreover, analysis of the deactivation kinetics during the tail activation protocol revealed a marked effect of A760G on channel deactivation. Evaluation of the deactivation kinetics during a transitions from 80 mV to multiple voltages near the foot of the activation curve provided an estimation of the kinetics of channels transitioning from fully open to closed (Fig. 1E,F). A double exponential function was used to quantify a fast and slow component of channel deactivation (τ_{fast}, τ_{slow} respectively). The A760G mutation significantly increased both time constants across voltages, indicating a considerable slowing of channel closing (Fig. 1J,K).

L-type channel S6 mutations have previously been shown to affect CDI via modulation of modal channel gating[14,38,57]. We therefore consider the underlying mechanism linking channel activation and CDI. An allosteric

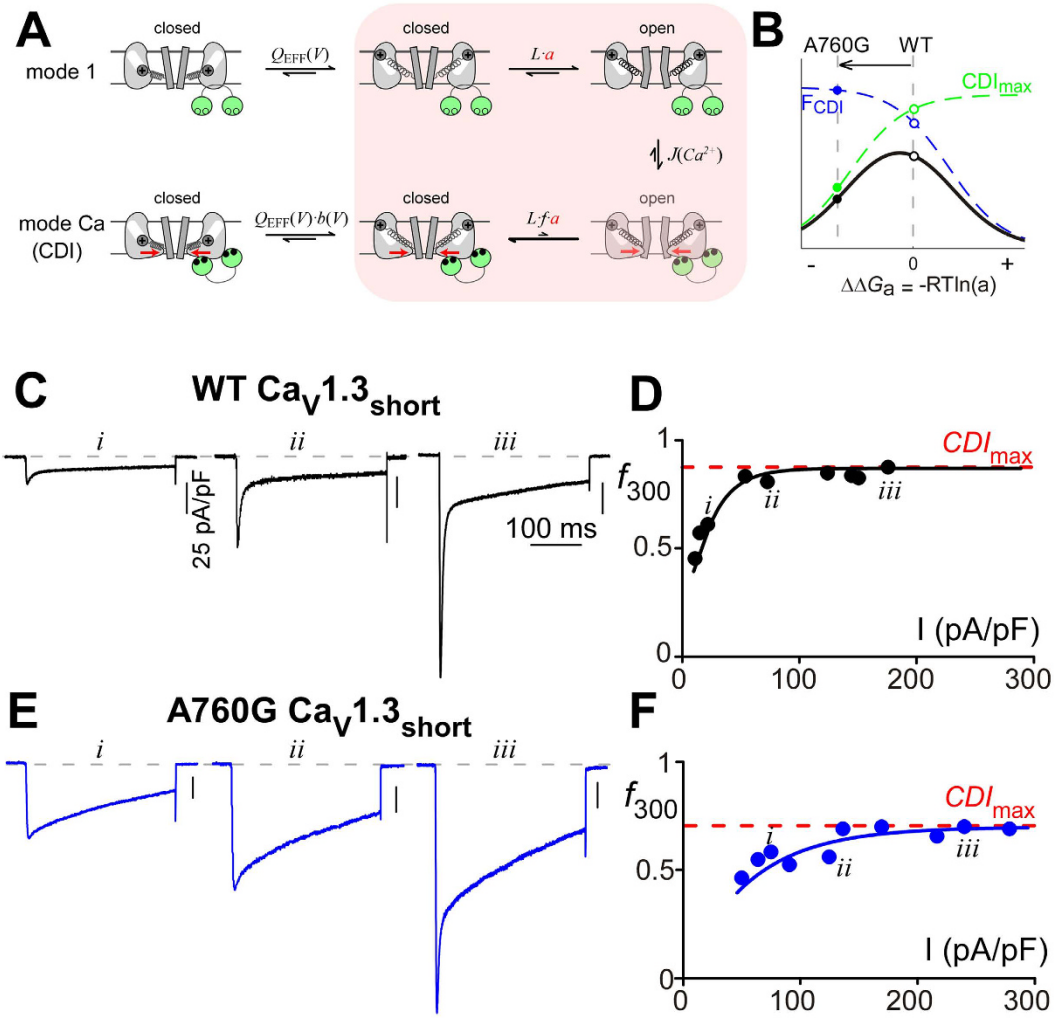

Figure 2. An allosteric mechanism underlying the CDI reduction. (**A**) Diagram representing an allosteric model of CDI. Channels transition from mode 1 with high P_O, to mode Ca^{2+} with lower P_O, in response to Ca^{2+} entry. Equilibrium constants Q_{EFF} (concerted movement of S1–S4 segments), L (S6 movement), and a (mutation effect) govern transitions between open and closed channel configurations[14,38], while the effective equilibrium constant $J(Ca^{2+})$ governs entry into mode Ca^{2+}. The parameter f ($0 < f < 1$) scales the P_O in mode Ca^{2+} resulting in CDI. State transitions expected to be effected by the A760G are shaded pink. (**B**) Total CDI (black), the product of F_{CDI} (blue) and CDI_{max} (green), is plotted as a function of $\Delta\Delta G_a$ for the model shown in panel A. The A760G mutation left-shifts voltage activation ($\Delta\Delta G_a < 0$, $a > 1$), predicting a decrease in CDI due to a decrease in CDI_{max}. (**C**) Exemplar Ca^{2+} current traces through WT $Ca_V1.3_{short}$ channels. Larger current amplitudes (*ii, iii*) allow a greater influx of Ca^{2+}, enhancing entry into mode Ca and thus increasing CDI as compared to diminutive Ca^{2+} currents (*i*). (**D**) f_{300} values for individual cells expressing WT $Ca_V1.3_{short}$ are plotted as a function of current density. The curve saturates at CDI_{max} ~0.9 (red dashed line). Traces in C correspond to *i–iii*. (**E**) Exemplar Ca^{2+} current traces through A760G $Ca_V1.3_{short}$ channels. Similar to that of WT (**C**), larger current amplitude increases f_{300} values. (**F**) Population data representing CDI of A760G $Ca_V1.3_{short}$ channels. f_{300} values saturate at CDI_{max} ~0.7 (red dashed line), significantly lower than WT.

model of channel gating (Fig. 2A) is known to describe CDI of $Ca_V1.3$ channels well[14]. Within this model, channels initially open within the mode 1 regime, which is characterized by a relatively large open probability ($P_{O/mode1}$). Upon channel opening, Ca^{2+} influx drives channels into the mode Ca regime where channels maintain the ability to open, but with a significantly reduced P_O ($P_{O/modeCa}$). It is this reduction in P_O that results in the CDI seen in whole-cell currents, such that

$$CDI = F_{CDI} * \frac{(P_{O/mode1} - P_{O/modeCa})}{P_{O/mode1}} \quad (1)$$

where F_{CDI} is the fraction of channels within mode Ca. Therefore at a saturating level of Ca^{2+}, F_{CDI} will approach unity as virtually all channels will reside within mode Ca. Under this condition, a maximal level of CDI (CDI_{max}) is achieved:

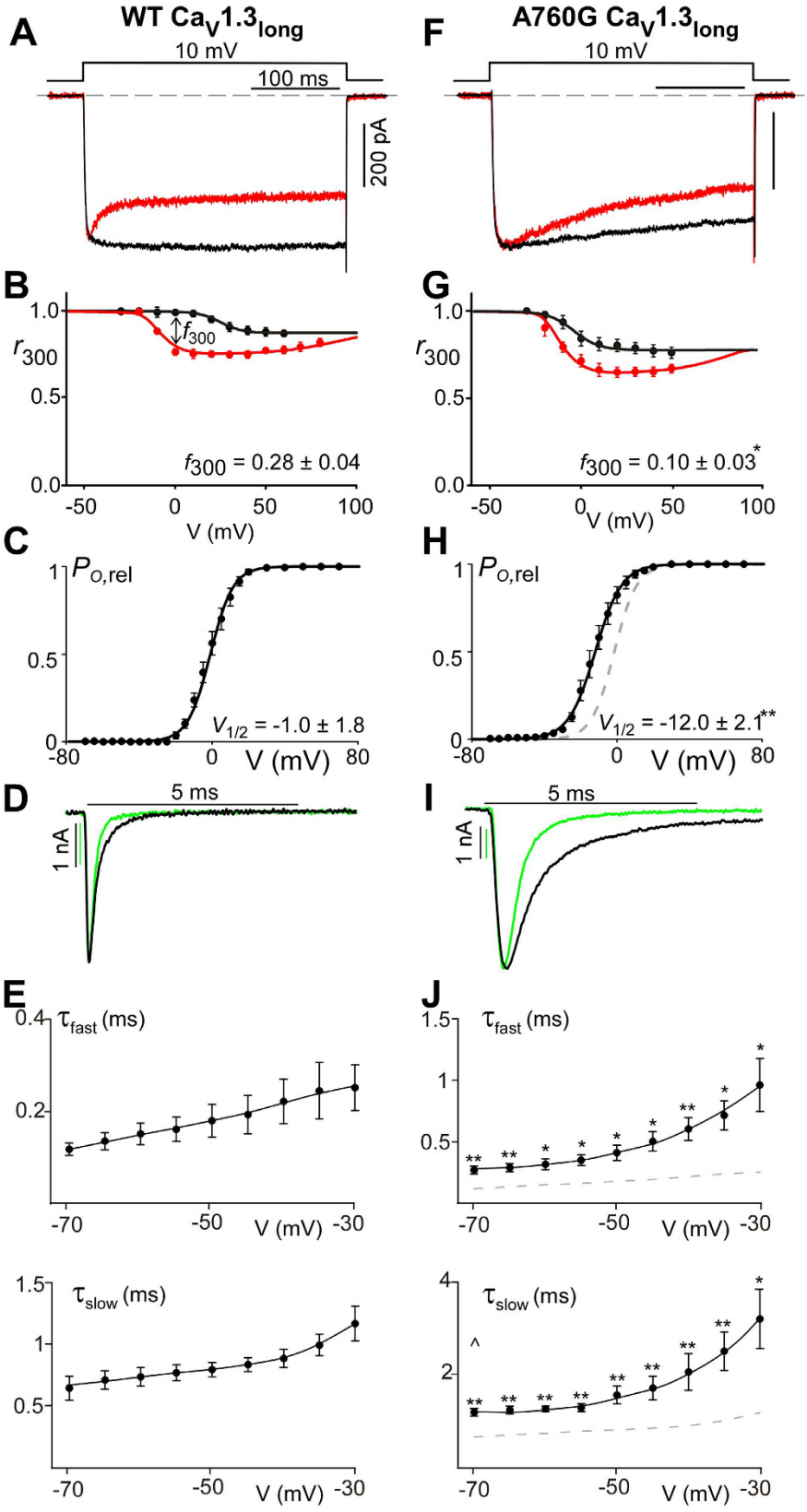

Figure 3. CDI reduction due to A760G mutation within the $Ca_V1.3$ long variant. (**A**) Exemplar Ca^{2+} (red) and Ba^{2+} (black) current traces through the alternate splice variant $Ca_V1.3_{long}$ illustrating decreased CDI as compared to the short splice variant (Fig. 1B). (**B**) Despite the reduction in magnitude, significant CDI is demonstrated by the difference in r_{300} for Ca^{2+} (red) and Ba^{2+} (black), plotted across multiple voltages. ($f_{300} = 0.28 \pm 0.04$, n = 3). (**C**) Voltage activation curve for Ba^{2+} current through WT $Ca_V1.3_{long}$ channels ($V_{1/2} = -1.0 \pm 1.8$ mV, n = 5). (**D**) Exemplar Ba^{2+} tail currents obtained from a transition from 80 mV

to −40 mV (black) and −60 mV (green). Traces are normalized to one another such that the scale bars correspond to the traces of the same color. (**E**) Population data of the fast (top) and slow (bottom) deactivation time constants (τ) plotted as a function of voltage. Error bars indicate ± SEM, n = 5. (**F**) Exemplar current traces through A760G $Ca_V1.3_{long}$ channels depicting diminished CDI as compared to WT channels. (**G**) Population data for r_{300} (red = Ca^{2+}, black = Ba^{2+}) plotted across multiple voltages ($f_{300} = 0.10 \pm 0.03$; n = 4, *p < 0.05). (**H**) The activation curve of A760G $Ca_V1.3_{long}$ channels (black, $V_{1/2} = -12.0 \pm 2.1$ mV, n = 4) shows an 11-mV hyperpolarizing shift (**p < 0.01) compared to WT (reproduced in gray for reference). (**I**) Exemplar Ba^{2+} tail currents for the A760G $Ca_V1.3_{long}$ channel, obtained from a transition from 80 mV to −40 mV (black) and −60 mV (green). Traces are normalized to one another such that the scale bars correspond to the traces of the same color. (**J**) Population data of the fast (top) and slow (bottom) deactivation time constants (τ) plotted as a function of voltage for the A760G $Ca_V1.3_{long}$ channel. Deactivation is significantly slowed as compared to WT reproduced as the gray dashed line (*p < 0.05, **p < 0.01). Error bars indicate ± SEM, n = 4.

$$CDI_{max} = \frac{(P_{O/mode1} - P_{O/modeCa})}{P_{O/mode1}} \quad (2)$$

We now consider the effects of the S6 mutation A760G within our model. As we and others[31] have shown that this mutation causes a hyperpolarizing shift in channel activation, the variable *a* was introduced to account for the altered free energy ($\Delta\Delta G_a$) required to open the mutant channels[14]. For a hyperpolarizing mutation such as A760G, $\Delta\Delta G_a$ will be negative, indicating decreased energy required to open the mutant channel. This decrease in free energy will result in increased channel opening in both mode 1 and mode Ca, thus decreasing CDI_{max} (Equation 2, Fig. 2B, green). This reduction of CDI_{max} could account for the overall decrease in CDI (Fig. 2B, black) observed in whole-cell experiments (Fig. 1), despite the increased F_{CDI} (Fig. 2B, blue) due to increased Ca^{2+} influx.

To test the hypothesis that the CDI deficit due to A760G is primarily a result of a decrease in CDI_{max}, we undertook whole-cell patch clamp recordings in which conditions enabled a sustained saturating level of Ca^{2+} at the mouth of the channel. By significantly reducing the intracellular Ca^{2+} buffer (0.5 mM EGTA), the accumulation of Ca^{2+} within the cell should overpower the nanodomain Ca^{2+} signal, thus raising Ca^{2+} to saturating levels as whole cell current increases[58] and providing an estimation of CDI_{max}[54]. For WT $Ca_V1.3$ channels, exemplar Ca^{2+} traces illustrate a saturating amount of CDI as a function of current density (Fig. 2C,D). The lack of additional CDI accumulation beyond a current density of 50 pA/pF indicates that we reached CDI_{max} at a value of ~0.9 for WT channels (Fig. 2D, red dashed line). A760G channels, however, demonstrate a significant reduction in CDI_{max} to ~0.7 (Fig. 2E,F), which can be observed at multiple test potentials (Supplementary Figure 2), confirming the underlying mechanism of CDI loss (Fig. 2B).

The A760G mutation differentially affects $Ca_V1.3$ splice variants. Ca_V channels are a critical conduit for Ca^{2+} entry into multiple cell types and must therefore be precisely tuned for specific cellular functions. Nature employs multiple mechanisms with which to accomplish such fine tuning, including modulation of channel splice patterns[3,17,22,23,59]. An example of such splicing in $Ca_V1.3$ channels results from inclusion of exon 42 or 42a, yielding a channel with a long versus short C-terminus[59]. The long channel variant activates at a somewhat more positive potential[3,24], has a lower open probability[15], and exhibits dramatically reduced CDI as compared to the short splice variant[3,16]. Due to these distinct properties, we examined the effect of the A760G mutation in both relevant splice variants. Having already demonstrated a significant reduction in CDI within the short channel variant, the isoform with more robust CDI[3,59] (Fig. 1), we next undertook a similar approach within the long $Ca_V1.3$ splice variant ($Ca_V1.3_{long}$).

Examination of CDI within the WT $Ca_V1.3_{long}$ channel under high buffering conditions (10 mM BAPTA) demonstrated significantly smaller, yet appreciable CDI (Fig. 3A,B), as compared to the short channel variant (Fig. 1B,C). Introduction of the A760G mutation blunted this CDI (Fig. 3F,G), though to a lesser extent as compared to the short variant. We next examined the activation of WT and A760G $Ca_V1.3_{long}$ channels. The resulting $P_{o,rel}$ versus voltage relationships (Fig. 3C,H) demonstrated an 11 mV hyperpolarizing shift due to the introduction of A760G ($p < 0.01$), similar to that observed in the short variant (Fig. 1D,I). Likewise, analysis of the deactivation kinetics also revealed a significant slowing of channel closing across multiple voltages (Fig. 3D,E,I,J). Thus, the biophysical deficits produced by the A760G mutation are qualitatively similar within each relevant channel backbone, although the magnitude of the CDI effect is somewhat decreased in the long splice variant.

Opposing VDI changes may mitigate the detrimental effects of A760G. In addition to the critical Ca^{2+}-dependent feedback, VDI also plays a major role in controlling Ca^{2+} entry through Ca_V1 channels. The underlying structural components for VDI have been shown to involve the linker region between domains I and II (I-II linker), which acts as a hinged-lid to close the pore following depolarization[14,48]. This process is known to be variably modulated by the binding of different isoforms of channel β subunits to the I-II linker[14,26]. For example, when coexpressed with β_{2a}, Ca_V1 channels display little VDI due to restricted movement caused by palmitoylation, and thus membrane anchoring, of the β_{2a} (Fig. 4A, blue)[28,51,52]. On the other hand, if the channels are coexpressed with the β_{1b} subunit, most Ca_V1 isoforms will display strong VDI due to the lack of the palmitoylation site[22,28]. $Ca_V1.3$ channels, however, are unique in that their S6 helices have been shown to act as a shield (Fig. 4A,D, red) to prevent closing of the I-II linker lid, thus, endowing the channels with minimal VDI regardless of β subunit isoform co-expressed.

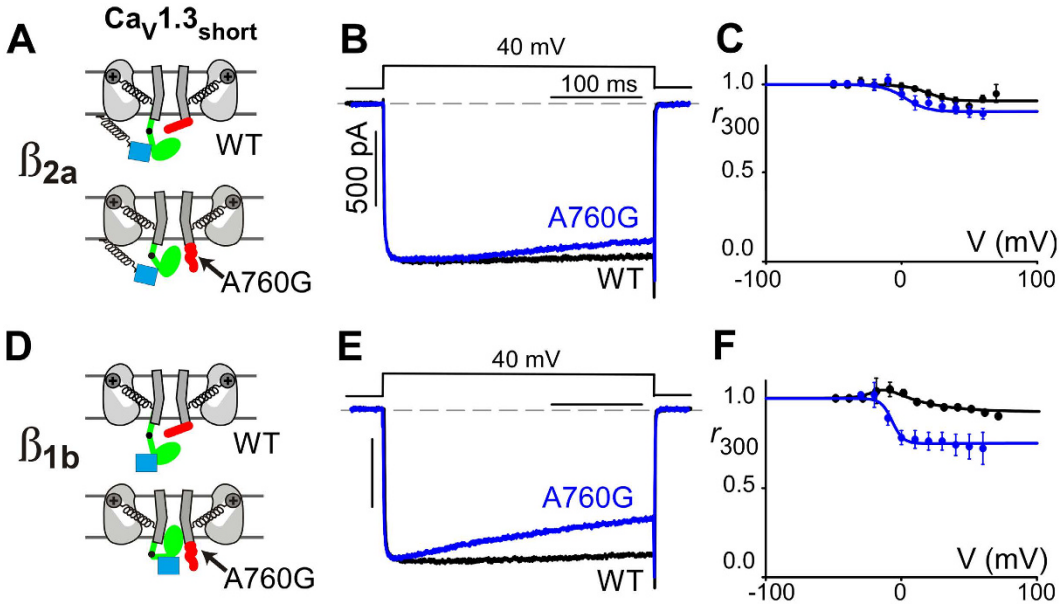

Figure 4. A760G increases VDI. (**A**) Cartoon depicting a β_{2a} subunit (blue) interacting with the VDI hinged lid (green) of a $Ca_V1.3_{short}$ channel. With palmitoylation, the β_{2a} subunit is anchored to the plasma membrane (black coil) restricting the movement of the channel hinged lid. $Ca_V1.3_{short}$ channels also possess a 'VDI shield' (red). The A760G mutation disrupts this shield (bottom). (**B**) Exemplar Ba^{2+} current through WT (black) and A760G (blue) $Ca_V1.3_{short}$ channels shows re-emergence of VDI even in the presence of β_{2a}. (**C**) Population data displaying Ba^{2+} r_{300} values as a function of voltage for WT (black) and A760G (blue). At 10 mV, WT: $r_{300} = 0.98 \pm 0.01$; n = 10; A760G: $r_{300} = 0.89 \pm 0.03$, n = 6. VDI is significantly increased in A760G channels ($p < 0.01$). (**D**) Cartoon depicting a β_{1b} subunit (blue) interacting with the hinged lid (green) of a $Ca_V1.3$ channel. Note the absence of palmitoylation of this β subunit which allows the VDI hinged lid to move freely. (**E**) Exemplar Ba^{2+} current trace through WT (black) and A760G (blue) $Ca_V1.3_{short}$ channels in the presence of β_{1b}. Note the absence of VDI in WT channels despite the lack of β subunit palmitoylation due to the presence of a VDI shield. A760G causes a pronounced re-emergence of VDI under these conditions. (**F**) The increase in VDI is confirmed in population data where Ba^{2+} r_{300} values for WT (black) and A760G (blue) are plotted as a function of voltage. At 10 mV, WT: $r_{300} = 0.98 \pm 0.01$, n = 3; A760G: $r_{300} = 0.77 \pm 0.05$, n = 4. VDI is significantly increased for A760G channels ($p < 0.01$).

A close inspection of the Ba^{2+} current through the A760G $Ca_V1.3$ channels reveals a slight, but significant re-emergence of VDI despite the presence of the β_{2a} subunit (Fig. 4B,C). Importantly, this mutation-induced VDI can be discerned in either of the two channel variants (Fig. 1G versus B, Fig. 3F versus A). This re-emergence of VDI is accentuated when A760G $Ca_V1.3$ is coexpressed with β subunits lacking a palmitoylation site. Figure 4E,F demonstrate a significant increase in VDI in channels harboring the A760G mutation in the presence of the β_{1b} subunit. Note that the WT $Ca_V1.3$ channels (black) have minimal VDI even in the presence of the β_{1b} subunit due to the existence of the 'shield'. Thus the re-emergence of VDI in these channels indicates that the A760G mutation may disrupt the VDI shield (Fig. 4A,D, bottom). This increase in VDI may act in opposition to the loss of CDI within these mutant channels, thus mitigating the detrimental effects of increased Ca^{2+} flux into cells.

The A760G mutation can cause an increase in intracellular Ca^{2+}. We now know that the A760G mutation has a significant effect on CDI, VDI, and deactivation. Given the known link between excess cytosolic Ca^{2+} and severe disease states[39,60,61], we wondered if Ca^{2+} overload due to an increased Ca^{2+} influx may play a role in the phenotype of A760G patients. However, the effects of the A760G mutation on Ca^{2+} entry are multi-fold, such that a decrease in CDI and slowing of channel deactivation are opposed by an increase in VDI. We therefore sought to confirm the cumulative effect of the A760G mutation on overall Ca^{2+} entry and intracellular Ca^{2+} concentration ($[Ca^{2+}]_i$).

To this end, we stimulated HEK293 cells expressing $Ca_V1.3$ channels with a 1-Hz train of neuronal action potentials (Fig. 5A, top) and recorded both the Ca^{2+} current passing through the channels as well as the intracellular Ca^{2+} level. This stimulation protocol was chosen as it matches well with the spontaneous neuronal firing frequencies in some populations of hippocampal neurons, thus mimicking a basal activity level[62,63]. When this protocol was applied to WT $Ca_V1.3$ channels, a small decrease in peak current amplitude was observed over time as CDI accumulated (Fig. 5A, middle panel). This amplitude decay matches well with the relatively small increase in $[Ca^{2+}]_i$ (Fig. 5A, bottom panel). When the A760G mutation was introduced into the channel, however, a significant increase in both the rate and extent of intracellular Ca^{2+} accumulation was observed (Fig. 5B–D, blue) due to an increased duration of Ca^{2+} entry during each action potential (Fig. 5B, left). This increased Ca^{2+} entry is likely a net result of decreased channel inactivation and a slowing of channel deactivation. This excess $[Ca^{2+}]_i$ increased the extent of CDI observed in the current recordings over time, although this decrease in current entry

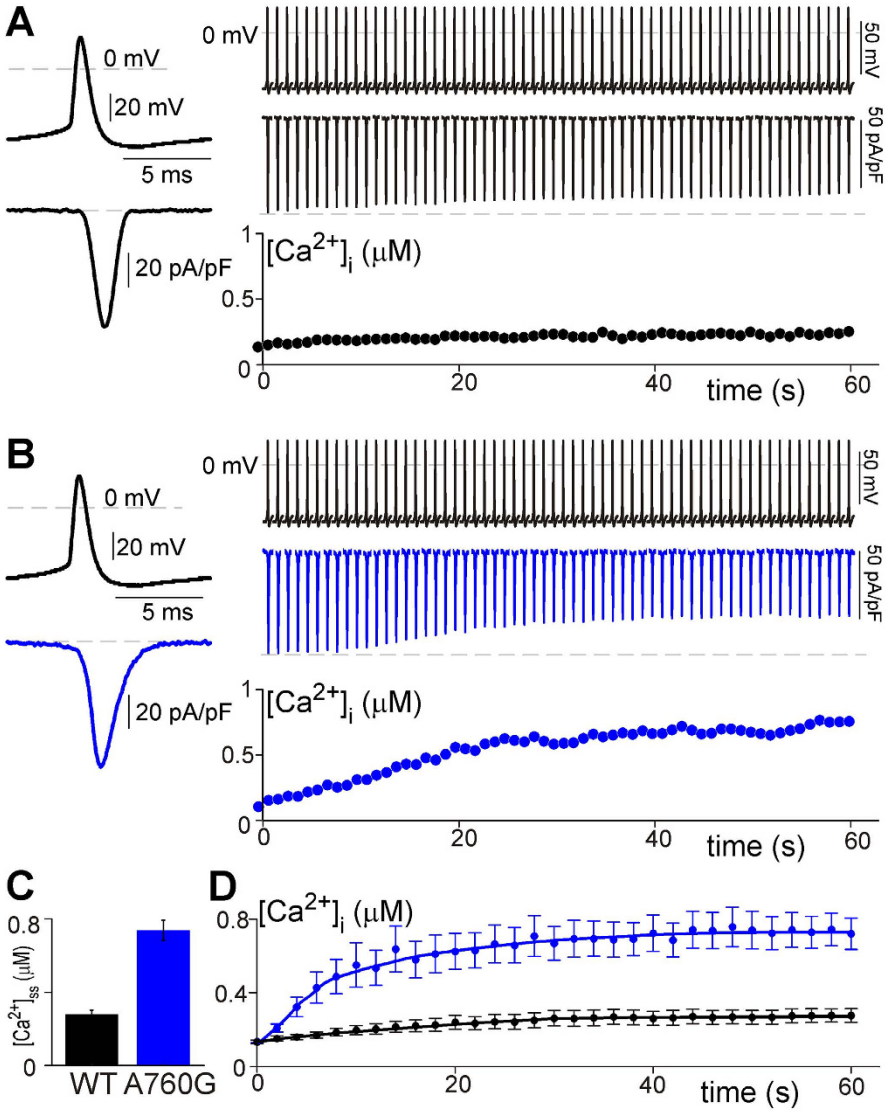

Figure 5. Effects of A760G on cytosolic Ca^{2+}. (**A**) Exemplar Ca^{2+} currents in response to a 1-Hz train of neuronal action potentials delivered to HEK293 cells expressing WT $Ca_V1.3_{short}$ channels. On the left, a single action potential and corresponding Ca^{2+} current is displayed on an expanded time course for resolution. Each action potential (top) and corresponding current response (middle) is magnified for display purposes and represents a 23 ms interval. The peak of each action potential is aligned with the time course displayed on the bottom panel. Note the gradual decrease in peak current as the level of cytosolic Ca^{2+} (bottom right panel) rises. (**B**) Exemplar Ca^{2+} currents in response to a 1-Hz train of neuronal action potentials delivered to HEK293 cells expressing A760G $Ca_V1.3_{short}$ channels. On the left, a magnified view demonstrates an increased duration of Ca^{2+} entry (blue) during a single action potential as compared to WT (**A**). At a comparable current density, A760G causes considerably more cytosolic Ca^{2+} accumulation (bottom right panel) as compared to WT channels. This increased cytosolic Ca^{2+} persists despite causing an enhancement of CDI (middle right panel). (**C**) Steady state level of intracellular Ca^{2+} in response to a 1-Hz train of action potentials. $[Ca^{2+}]_{ss}$ is measured after 60 s of stimulation. A760G $Ca_V1.3$ channels display significantly higher levels of $[Ca^{2+}]_{ss}$ than WT channels (WT: 0.28 ± 0.05, $n = 7$; A760G: 0.73 ± 0.13, $n = 8$; $p < 0.01$). (**D**) Average $[Ca^{2+}]_i$ as a function of time as HEK293 cells expressing WT or A760G $Ca_V1.3_{short}$ channels are stimulated by a train of 1-Hz action potential. Error bars indicate ± SEM, $n = 7, 8$ for WT and A760G respectively.

was not sufficient to counteract the Ca^{2+} overload within the cytosol. Overall, the cumulative effect was a steady state Ca^{2+} level approaching 0.8 uM (Fig. 5C), substantially larger than the normal resting $[Ca^{2+}]_i$ of a neuron[64]. This excess cytosolic Ca^{2+} due to A760G could be a significant contributing factor to the disease pathogenesis.

Discussion

We have demonstrated a significant effect of the autism-associated mutation A760G on the gating of $Ca_V1.3$ such that channel activation is significantly left-shifted, CDI is decreased, and deactivation is slowed, resulting in

excess Ca^{2+} entry through channels. However, these effects are mitigated by an increase in VDI. Importantly, the balance between these opposing mechanisms may be dependent on the specific properties of the particular channel complex harboring the mutation. In particular, we have demonstrated that two major $Ca_V1.3$ splice variants respond to the introduction of the A760G mutation with distinct levels of CDI disruption (Figs 1 and 3). As each of these splice variants has a significantly different affinity for commonly used L-type channel blockers[59], such a variation in CDI effects may have important implications on the response of patients to treatment. Moreover, these two splice variants represent only a subset of a panoply of channel isoforms found across different tissues, each with uniquely tuned channel gating and feedback regulation[3,11,17–19,59]. Like the short versus long splice isoforms, it is possible that the A760G mutation may differentially alter the biophysical properties of these variants. Thus the extent of channel alteration may depend on the expression pattern within each specific cell type resulting in variable phenotypes across different tissues.

The original case report for A760G describes a patient exhibiting primarily neurological deficits classified as ASD[30]. Upon further examination of the Simons Simplex Collection database, the classification of ASD in this proband appeared to be of a relatively milder nature on the autism spectrum (pervasive developmental disorder not otherwise specified or PDD NOS) without additional non-neurological symptoms. Such a narrow symptom profile without any cardiac or hearing deficits stands in contrast to the broad tissue distribution of $Ca_V1.3$. Moreover, this lack of severe multisystem characteristics is unusual for autism-related Ca^{2+} channelopathies[29,39,40,65]. The multitude of $Ca_V1.3$ channel variants across different tissues[17,22,23] may account for some of this lack of a multi-system phenotype. The relatively moderate symptoms of this proband may be due, in part, to differential effects of the A760G mutation on specific channel variants expressed in each system. In addition, the VDI effects of the A760G mutation could also contribute to the milder phenotype displayed by the proband. In particular, the increased Ca^{2+} entry due to altered CDI and channel activation/deactivation may be partially offset by increased VDI. As this VDI enhancement is accentuated in the presence of select beta subunits (Fig. 4), expression patterns of different beta subunits[66] may further increase the variability of A760G effects across systems.

The A760G mutation is capable of substantially raising cytosolic Ca^{2+} concentration when overexpressed in HEK293 cells (Fig. 5). Of note, this effect was achieved even at a relatively slow 1-Hz pacing rate, comparable to the spontaneous firing rate of some hippocampal neurons[62,63]. The experimental conditions utilized here were optimized for maximal resolution of the A760G effect. However, under physiological heterozygous expression levels, the effect of the A760G channels will likely be considerably less. Nonetheless, the idea of excessive Ca^{2+} entry underlying ASD is not unprecedented as the ASD phenotype has been linked to Ca^{2+} overload through a myriad of Ca^{2+} handling molecules[67–69], including multiple voltage-gated Ca^{2+} channels[39,40,65,70]. Overall, it seems plausible that the gating defects of the $Ca_V1.3$ channels harboring the A760G mutation may result in excess Ca^{2+} entry, which in turn may be over-activating the downstream Ca^{2+} signaling pathways involved in neural development and plasticity[67–70]. While the mechanisms underlying ASD remain elusive, the identification of mutations such as A760G, hint at important contributing factors.

Methods

Molecular Biology. The point mutation (A760G) was introduced into rat $Ca_V1.3$ short and long splice variants (gifts from Dr. Tuck Wah Soong[59]) in the homologous position to that found in humans using QuikChange™ site-directed mutagenesis (Agilent). The equivalent human mutation was found in patients at A769G in chromosome 3, position 53764493[30] and corresponds to the A749G mutation previously described in an alternate human splice variant[31].

Transfection of HEK293 cells. HEK293 cells were cultured on glass coverslips in 10-cm dishes and WT or mutant $Ca_V1.3$ channels, along with their auxiliary subunits, were transiently transfected using a standard calcium phosphate method[71]. 8 μg of rat $Ca_V1.3$ was co-expressed with 8 μg of rat brain β_{2a} (M80545) or β_{1b} (NM_017346), 8 μg of rat brain $\alpha_2\delta$ (NM012919.2) subunits, and 2 μg of simian virus 40 T antigen cDNA. Expression of all constructs was driven by a cytomegalovirus promoter and β subunits were contained within an EGFP-IRES bicistronic vector to allow visualization of transfected cells.

Whole Cell Electrophysiology. Whole-cell voltage-clamp recordings of HEK293 cells were done 1–2 days after transfection at room temperature. Recordings were obtained using an Axopatch 200B amplifier (Axon Instruments). Whole-cell voltage-clamp records were low pass filtered at 2 kHz, and then digitally sampled at 10 kHz. P/8 leak subtraction was used, with series resistances of 1–2 MΩ. For voltage-clamp experiments, internal solutions contained (in mM): $CsMeSO_3$, 114; CsCl, 5; $MgCl_2$, 1; MgATP, 4; HEPES (pH 7.3), 10; and either BAPTA, 10 or EGTA, 0.5; at 295 mOsm adjusted with $CsMeSO_3$. External solutions contained (in mM): TEA-$MeSO_3$, 140; HEPES (pH 7.4), 10; and $CaCl_2$ or $BaCl_2$, 40; at 300 mOsm, adjusted with TEA-$MeSO_3$.

For simultaneous ratiometric Ca^{2+} measurements and current recordings, a fixed ratio of two Ca^{2+}-sensitive dyes (Fluo-2 high affinity, TEFLabs; Fluo-2 low affinity, TEFLabs) and Alexa568 (Invitrogen) were added into a 0.5-mM EGTA internal solution. Two Ca^{2+} indicators at different binding affinity were chosen to accurately measure both baseline and peak Ca^{2+} concentrations. The dye mixture was calibrated to obtain absolute Ca^{2+} concentrations[72]. The external solution (Tyrode's solution) contained (in mM): NaCl, 135; KCl, 5.4; $CaCl_2$, 1.8; $MgCl_2$, 0.33; NaH_2PO_4, 0.33; HEPES, 5; glucose, 5 (pH 7.4). During current recordings, Ca^{2+} concentration was measured by exciting dyes using a 514-nm Argon laser, via a 545DCLP dichroic mirror and either a 545/40BP (Fluo) or 580LP (Alexa568) filter. Cells were held at −80 mV and a 1-Hz train of neuronal action potential recordings from cortical neurons of E18 mouse embryos were used as voltage stimulus.

Generation of a $Ca_V1.3$ Homology Model. We used MODELLER v9.14[73] to build a homology model of $Ca_V1.3$ pore regions (Fig. 1A) based on the crystal structure of the bacterial Na channel Na_VAb (PDB accession code: 4EKW)[74] as previously described[14]. Briefly, we generated 10 decoy models from which a model with lower objective function was chosen. The four domains of $Ca_V1.3$ were constrained to adopt a clockwise orientation when viewed from the extracellular surface by analogy to the orientation of the related voltage-gated sodium channels[75]. The alignment used for the various pore subsegments are as follows:

S5 Segment	
Na_VAb	SVAALLTVVFYIAAVMATNLYGATFP
$Ca_V1.3$ Domain I	HIALLVLFVIIIYAIIGLELFIGKMH
$Ca_V1.3$ Domain II	SLLLLLFLFIIIFSLLGMQLFGGKFN
$Ca_V1.3$ Domain III	NIMIVTTLLQFMFACIGVQLFKGKFY
$Ca_V1.3$ Domain IV	YVALLIAMLFFIYAVIGMQMFGKVAM
P Loop	
Na_VAb	EWFGDLSKSLYTLFQVMTLESWSMGIVRPVMNV
$Ca_V1.3$ Domain I	TNFDNFAFAMLTVFQCITMEGWTDVLYWVNDAI
$Ca_V1.3$ Domain II	STFDNFPQALLTVFQILTGEDWNAVMYDGIMAY
$Ca_V1.3$ Domain III	FNFDNVLSAMMVLFTVSTFEGWPALLYKAIDSN
Ca_{V1}.3 Domain IV	NNFQTFPQAVLLLFRCATGEAWQEIMLACLPGK
S6 Segment	
Na_VAb	HPNAWVFFIPFIMLTTFTVLNLFIGII
$Ca_V1.3$ Domain I	WEWPWVYFVSLIILGSFFVLNLVLGVL
$Ca_V1.3$ Domain II	GMIVCIYFIILFICGNYILLNVFLAIA
$Ca_V1.3$ Domain III	RVEISIFFIIYIIIVAFFMMNIFVGFV
$Ca_V1.3$ Domain IV	SNFAIVYFISFYMLCAFLIINLFVAVI

Data Analysis and Statistics. The fraction of current remaining after 300 ms of channel activation (r_{300}) was calculated as:

$$r_{300} = \frac{I(300)}{I(t_{peak})} \tag{3}$$

and CDI measurements were corrected for VDI effects by calculating a metric for pure CDI (f_{300}) as follows:

$$f_{300} = \frac{r_{300}^{Ba} - r_{300}^{Ca}}{r_{300}^{Ba}} \tag{4}$$

r_{300} and f_{300} values were reported at 10 mV for the $Ca_V1.3_{short}$ channel and at 0 mV for $Ca_V1.3_{long}$. The relative open probability ($P_{O,rel}$) was determined by a tail activation protocol[54] where channels are fully activated at 80 mV prior to stepping to variable test potentials. The ratio of peak and steady state currents then represent the relative $P_{O,rel}$ of each voltage. The voltage activation curve was fit by the Boltzmann equation:

$$P_{O,rel} = scale * \left(1 + e^{-\frac{V - V_{1/2}}{k}}\right)^{-1} \tag{5}$$

where $V_{1/2}$ and k represent the half activation voltage and slope factor, respectively.

Time constants for channel deactivation (τ_{fast} and τ_{slow} in Figs 1F,K and 3E,J) were calculated by fitting the deactivating Ba^{2+} tail currents resulting from a transition from 80 mV (channels maximally open based on the activation curve, Figs 1D,I and 3C,H) to multiple voltages near the base of the activation curve (channels closed) with the equation:

$$I_{fit} = A * \left(f * e^{-\left(\frac{t - t_0}{\tau_{fast}}\right)} + (1 - f) * e^{-\left(\frac{t - t_0}{\tau_{slow}}\right)}\right) \tag{6}$$

where f is the fraction of the faster portion of the current decay, and time constants τ_{fast} and τ_{slow} represent the fast and slow components of the current decay.

All data are presented as mean ± SEM. Statistical significance for variability was determined by a two-tailed student's t-test.

References

1. Berger, S. M. & Bartsch, D. The role of L-type voltage-gated calcium channels $Ca_v1.2$ and $Ca_v1.3$ in normal and pathological brain function. *Cell Tissue Res.* **357,** 463–476, doi: 10.1007/s00441-014-1936-3 (2014).
2. Pinggera, A. & Striessnig, J. Ca 1.3 (CACNA1D) L-type Ca channel dysfunction in CNS disorders. *J. Physiol.*, doi: 10.1113/JP270672 (2016).
3. Striessnig, J., Pinggera, A., Kaur, G., Bock, G. & Tuluc, P. L-type Ca channels in heart and brain. *Wiley Interdiscip Rev Membr Transp Signal* **3,** 15–38, doi: 10.1002/wmts.102 (2014).

4. Zamponi, G. W., Striessnig, J., Koschak, A. & Dolphin, A. C. The Physiology, Pathology, and Pharmacology of Voltage-Gated Calcium Channels and Their Future Therapeutic Potential. *Pharmacol. Rev.* **67,** 821–870, doi: 10.1124/pr.114.009654 (2015).
5. Mesirca, P., Torrente, A. G. & Mangoni, M. E. Functional role of voltage gated Ca(2+) channels in heart automaticity. *Front. Physiol.* **6,** 19, doi: 10.3389/fphys.2015.00019 (2015).
6. Barrett, P. Q. *et al.* Role of voltage-gated calcium channels in the regulation of aldosterone production from zona glomerulosa cells of the adrenal cortex. *J. Physiol.*, doi: 10.1113/JP271896 (2016).
7. Marcantoni, A. *et al.* L-type calcium channels in adrenal chromaffin cells: role in pace-making and secretion. *Cell Calcium* **42,** 397–408, doi: 10.1016/j.ceca.2007.04.015 (2007).
8. Xu, W. & Lipscombe, D. Neuronal Ca(V)1.3alpha(1) L-type channels activate at relatively hyperpolarized membrane potentials and are incompletely inhibited by dihydropyridines. *J. Neurosci.* **21,** 5944–5951 (2001).
9. Koschak, A. *et al.* alpha 1D ($Ca_v1.3$) subunits can form l-type Ca^{2+} channels activating at negative voltages. *J. Biol. Chem.* **276,** 22100–22106, doi: 10.1074/jbc.M101469200 (2001).
10. Lipscombe, D., Andrade, A. & Allen, S. E. Alternative splicing: functional diversity among voltage-gated calcium channels and behavioral consequences. *Biochim. Biophys. Acta* **1828,** 1522–1529, doi: 10.1016/j.bbamem.2012.09.018 (2013).
11. Lieb, A., Ortner, N. & Striessnig, J. C-terminal modulatory domain controls coupling of voltage-sensing to pore opening in $Ca_v1.3$ L-type Ca(2+) channels. *Biophys. J.* **106,** 1467–1475, doi: 10.1016/j.bpj.2014.02.017 (2014).
12. Scholze, A., Plant, T. D., Dolphin, A. C. & Nurnberg, B. Functional expression and characterization of a voltage-gated $Ca_v1.3$ (alpha1D) calcium channel subunit from an insulin-secreting cell line. *Mol. Endocrinol.* **15,** 1211–1221, doi: 10.1210/mend.15.7.0666 (2001).
13. Satin, J., Schroder, E. A. & Crump, S. M. L-type calcium channel auto-regulation of transcription. *Cell Calcium* **49,** 306–313, doi: 10.1016/j.ceca.2011.01.001 (2011).
14. Tadross, M. R., Ben Johny, M. & Yue, D. T. Molecular endpoints of Ca^{2+}/calmodulin- and voltage-dependent inactivation of Ca(v)1.3 channels. *J. Gen. Physiol.* **135,** 197–215, doi: 10.1085/jgp.200910308 (2010).
15. Adams, P. J., Ben-Johny, M., Dick, I. E., Inoue, T. & Yue, D. T. Apocalmodulin itself promotes ion channel opening and Ca(2+) regulation. *Cell* **159,** 608–622, doi: 10.1016/j.cell.2014.09.047 (2014).
16. Liu, X., Yang, P. S., Yang, W. & Yue, D. T. Enzyme-inhibitor-like tuning of Ca(2+) channel connectivity with calmodulin. *Nature* **463,** 968–972, doi: 10.1038/nature08766 (2010).
17. Tan, B. Z. *et al.* Functional characterization of alternative splicing in the C terminus of L-type $Ca_v1.3$ channels. *J. Biol. Chem.* **286,** 42725–42735, doi: 10.1074/jbc.M111.265207 (2011).
18. Bazzazi, H., Ben Johny, M., Adams, P. J., Soong, T. W. & Yue, D. T. Continuously tunable Ca(2+) regulation of RNA-edited $Ca_v1.3$ channels. *Cell Rep* **5,** 367–377, doi: 10.1016/j.celrep.2013.09.006 (2013).
19. Huang, H. *et al.* RNA editing of the IQ domain in Ca(v)1.3 channels modulates their Ca(2)(+)-dependent inactivation. *Neuron* **73,** 304–316, doi: 10.1016/j.neuron.2011.11.022 (2012).
20. Roberts-Crowley, M. L. & Rittenhouse, A. R. Arachidonic acid inhibition of L-type calcium ($Ca_v1.3b$) channels varies with accessory Ca_vbeta subunits. *J. Gen. Physiol.* **133,** 387–403, doi: 10.1085/jgp.200810047 (2009).
21. Dolphin, A. C. Calcium channel diversity: multiple roles of calcium channel subunits. *Curr. Opin. Neurobiol.* **19,** 237–244, doi: 10.1016/j.conb.2009.06.006 (2009).
22. Shen, Y. *et al.* Alternative splicing of the Ca(v)1.3 channel IQ domain, a molecular switch for Ca^{2+}-dependent inactivation within auditory hair cells. *J. Neurosci.* **26,** 10690–10699, doi: 10.1523/JNEUROSCI.2093-06.2006 (2006).
23. Bock, G. *et al.* Functional properties of a newly identified C-terminal splice variant of $Ca_v1.3$ L-type Ca^{2+} channels. *J. Biol. Chem.* **286,** 42736–42748, doi: 10.1074/jbc.M111.269951 (2011).
24. Singh, A. *et al.* Modulation of voltage- and Ca^{2+}-dependent gating of $Ca_v1.3$ L-type calcium channels by alternative splicing of a C-terminal regulatory domain. *J. Biol. Chem.* **283,** 20733–20744, doi: 10.1074/jbc.M802254200 (2008).
25. Dolphin, A. C. Calcium channel auxiliary alpha2delta and beta subunits: trafficking and one step beyond. *Nat. Rev. Neurosci.* **13,** 542–555, doi: 10.1038/nrn3311 (2012).
26. Buraei, Z. & Yang, J. Structure and function of the beta subunit of voltage-gated Ca(2)(+) channels. *Biochim. Biophys. Acta* **1828,** 1530–1540, doi: 10.1016/j.bbamem.2012.08.028 (2013).
27. Dolphin, A. C. Beta subunits of voltage-gated calcium channels. *J. Bioenerg. Biomembr.* **35,** 599–620 (2003).
28. Colecraft, H. M. *et al.* Novel functional properties of Ca(2+) channel beta subunits revealed by their expression in adult rat heart cells. *J. Physiol.* **541,** 435–452 (2002).
29. Breitenkamp, A. F., Matthes, J. & Herzig, S. Voltage-gated Calcium Channels and Autism Spectrum Disorders. *Curr. Mol. Pharmacol.* **8,** 123–132 (2015).
30. O'Roak, B. J. *et al.* Sporadic autism exomes reveal a highly interconnected protein network of de novo mutations. *Nature* **485,** 246–250, doi: 10.1038/nature10989 (2012).
31. Pinggera, A. *et al.* CACNA1D de novo mutations in autism spectrum disorders activate $Ca_v1.3$ L-type calcium channels. *Biol. Psychiatry* **77,** 816–822, doi: 10.1016/j.biopsych.2014.11.020 (2015).
32. Baig, S. M. *et al.* Loss of Ca(v)1.3 (CACNA1D) function in a human channelopathy with bradycardia and congenital deafness. *Nat. Neurosci.* **14,** 77–84, doi: 10.1038/nn.2694 (2011).
33. Platzer, J. *et al.* Congenital deafness and sinoatrial node dysfunction in mice lacking class D L-type Ca^{2+} channels. *Cell* **102,** 89–97 (2000).
34. Azizan, E. A. *et al.* Somatic mutations in ATP1A1 and CACNA1D underlie a common subtype of adrenal hypertension. *Nat. Genet.* **45,** 1055–1060, doi: 10.1038/ng.2716 (2013).
35. Scholl, U. I. *et al.* Somatic and germline CACNA1D calcium channel mutations in aldosterone-producing adenomas and primary aldosteronism. *Nat. Genet.* **45,** 1050–1054, doi: 10.1038/ng.2695 (2013).
36. Dou, H. *et al.* Null mutation of alpha1D Ca^{2+} channel gene results in deafness but no vestibular defect in mice. *J Assoc Res Otolaryngol* **5,** 215–226, doi: 10.1007/s10162-003-4020-3 (2004).
37. Iossifov, I. *et al.* De novo gene disruptions in children on the autistic spectrum. *Neuron* **74,** 285–299, doi: 10.1016/j.neuron.2012.04.009 (2012).
38. Dick, I. E., Joshi-Mukherjee, R., Yang, W & Yue, D. T. Arrhythmogenesis in Timothy Syndrome is associated with defects in Ca^{2+} dependent inactivation. *Nat Commun* **7,** 10370, doi: 10.1038/ncomms10370 (2016).
39. Splawski, I. *et al.* Severe arrhythmia disorder caused by cardiac L-type calcium channel mutations. *Proc. Natl. Acad. Sci. USA* **102,** 8089–8096; discussion 8086-8088, doi: 10.1073/pnas.0502506102 (2005).
40. Splawski, I. *et al.* Ca(V)1.2 calcium channel dysfunction causes a multisystem disorder including arrhythmia and autism. *Cell* **119,** 19–31, doi: 10.1016/j.cell.2004.09.011 (2004).
41. Limpitikul, W. B. *et al.* Calmodulin mutations associated with long QT syndrome prevent inactivation of cardiac L-type Ca(2+) currents and promote proarrhythmic behavior in ventricular myocytes. *J. Mol. Cell. Cardiol.* **74,** 115–124, doi: 10.1016/j.yjmcc.2014.04.022 (2014).
42. Hoda, J. C., Zaghetto, F., Koschak, A. & Striessnig, J. Congenital stationary night blindness type 2 mutations S229P, G369D, L1068P, and W1440X alter channel gating or functional expression of Ca(v)1.4 L-type Ca^{2+} channels. *J. Neurosci.* **25,** 252–259, doi: 10.1523/JNEUROSCI.3054-04.2005 (2005).

43. Hohaus, A. *et al.* Structural determinants of L-type channel activation in segment IIS6 revealed by a retinal disorder. *J. Biol. Chem.* **280,** 38471–38477, doi: 10.1074/jbc.M507013200 (2005).
44. Kraus, R. L. *et al.* Three new familial hemiplegic migraine mutants affect P/Q-type Ca(2+) channel kinetics. *J. Biol. Chem.* **275,** 9239–9243 (2000).
45. Raybaud, A. *et al.* The role of distal S6 hydrophobic residues in the voltage-dependent gating of $Ca_v2.3$ channels. *J. Biol. Chem.* **282,** 27944–27952, doi: 10.1074/jbc.M703895200 (2007).
46. Raybaud, A. *et al.* The role of the GX9GX3G motif in the gating of high voltage-activated Ca^{2+} channels. *J. Biol. Chem.* **281,** 39424–39436, doi: 10.1074/jbc.M607405200 (2006).
47. Barrett, C. F. & Tsien, R. W. The Timothy syndrome mutation differentially affects voltage- and calcium-dependent inactivation of $Ca_v1.2$ L-type calcium channels. *Proc. Natl. Acad. Sci. USA* **105,** 2157–2162, doi: 10.1073/pnas.0710501105 (2008).
48. Stotz, S. C., Hamid, J., Spaetgens, R. L., Jarvis, S. E. & Zamponi, G. W. Fast inactivation of voltage-dependent calcium channels. A hinged-lid mechanism? *J. Biol. Chem.* **275,** 24575–24582, doi: 10.1074/jbc.M000399200 (2000).
49. Stotz, S. C., Jarvis, S. E. & Zamponi, G. W. Functional roles of cytoplasmic loops and pore lining transmembrane helices in the voltage-dependent inactivation of HVA calcium channels. *J. Physiol.* **554,** 263–273, doi: 10.1113/jphysiol.2003.047068 (2004).
50. Stotz, S. C. & Zamponi, G. W. Identification of inactivation determinants in the domain IIS6 region of high voltage-activated calcium channels. *J. Biol. Chem.* **276,** 33001–33010, doi: 10.1074/jbc.M104387200 (2001).
51. Dafi, O. *et al.* Negatively charged residues in the N-terminal of the AID helix confer slow voltage dependent inactivation gating to $Ca_v1.2$. *Biophys. J.* **87,** 3181–3192, doi: 10.1529/biophysj.104.045559 (2004).
52. Stea, A. *et al.* Localization and functional properties of a rat brain alpha 1A calcium channel reflect similarities to neuronal Q- and P-type channels. *Proc. Natl. Acad. Sci. USA* **91,** 10576–10580 (1994).
53. Dick, I. E. *et al.* A modular switch for spatial Ca^{2+} selectivity in the calmodulin regulation of Ca_v channels. *Nature* **451,** 830–834, doi: 10.1038/nature06529 (2008).
54. Tadross, M. R., Dick, I. E. & Yue, D. T. Mechanism of local and global Ca^{2+} sensing by calmodulin in complex with a Ca^{2+} channel. *Cell* **133,** 1228–1240, doi: 10.1016/j.cell.2008.05.025 (2008).
55. Brehm, P. & Eckert, R. Calcium entry leads to inactivation of calcium channel in Paramecium. *Science* **202,** 1203–1206 (1978).
56. Brehm, P., Eckert, R. & Tillotson, D. Calcium-mediated inactivation of calcium current in Paramecium. *J. Physiol.* **306,** 193–203 (1980).
57. Imredy, J. P. & Yue, D. T. Mechanism of Ca(2+)-sensitive inactivation of L-type Ca^{2+} channels. *Neuron* **12,** 1301–1318 (1994).
58. Yang, P. S. *et al.* Switching of Ca^{2+}-dependent inactivation of Ca(v)1.3 channels by calcium binding proteins of auditory hair cells. *J. Neurosci.* **26,** 10677–10689, doi: 10.1523/JNEUROSCI.3236-06.2006 (2006).
59. Huang, H., Yu, D. & Soong, T. W. C-terminal alternative splicing of $Ca_v1.3$ channels distinctively modulates their dihydropyridine sensitivity. *Mol. Pharmacol.* **84,** 643–653, doi: 10.1124/mol.113.087155 (2013).
60. Schulz, J. B. Mechanisms of neurodegeneration in idiopathic Parkinson's disease. *Parkinsonism Relat. Disord.* **13** Suppl 3, S306–308, doi: 10.1016/S1353-8020(08)70021-X (2007).
61. Zhang, L., Yang, H., Zhao, H. & Zhao, C. Calcium-related signaling pathways contributed to dopamine-induced cortical neuron apoptosis. *Neurochem. Int.* **58,** 281–294, doi: 10.1016/j.neuint.2010.11.021 (2011).
62. Mizuseki, K. & Buzsaki, G. Preconfigured, skewed distribution of firing rates in the hippocampus and entorhinal cortex. *Cell Rep* **4,** 1010–1021, doi: 10.1016/j.celrep.2013.07.039 (2013).
63. Hirase, H., Leinekugel, X., Czurko, A., Csicsvari, J. & Buzsaki, G. Firing rates of hippocampal neurons are preserved during subsequent sleep episodes and modified by novel awake experience. *Proc. Natl. Acad. Sci. USA* **98,** 9386–9390, doi: 10.1073/pnas.161274398 (2001).
64. Verkhratsky, A., Shmigol, A., Kirischuk, S., Pronchuk, N. & Kostyuk, P. Age-dependent changes in calcium currents and calcium homeostasis in mammalian neurons. *Ann. N. Y. Acad. Sci.* **747,** 365–381 (1994).
65. Hemara-Wahanui, A. *et al.* A CACNA1F mutation identified in an X-linked retinal disorder shifts the voltage dependence of $Ca_v1.4$ channel activation. *Proc. Natl. Acad. Sci. USA* **102,** 7553–7558, doi: 10.1073/pnas.0501907102 (2005).
66. Ludwig, A., Flockerzi, V. & Hofmann, F. Regional expression and cellular localization of the alpha1 and beta subunit of high voltage-activated calcium channels in rat brain. *J. Neurosci.* **17,** 1339–1349 (1997).
67. Barnby, G. *et al.* Candidate-gene screening and association analysis at the autism-susceptibility locus on chromosome 16p: evidence of association at GRIN2A and ABAT. *Am. J. Hum. Genet.* **76,** 950–966, doi: 10.1086/430454 (2005).
68. Chen, W. G. *et al.* Derepression of BDNF transcription involves calcium-dependent phosphorylation of MeCP2. *Science* **302,** 885–889, doi: 10.1126/science.1086446 (2003).
69. Zhou, Z. *et al.* Brain-specific phosphorylation of MeCP2 regulates activity-dependent Bdnf transcription, dendritic growth, and spine maturation. *Neuron* **52,** 255–269, doi: 10.1016/j.neuron.2006.09.037 (2006).
70. Krey, J. F. & Dolmetsch, R. E. Molecular mechanisms of autism: a possible role for Ca^{2+} signaling. *Curr. Opin. Neurobiol.* **17,** 112–119, doi: 10.1016/j.conb.2007.01.010 (2007).
71. Peterson, B. Z., DeMaria, C. D., Adelman, J. P. & Yue, D. T. Calmodulin is the Ca^{2+} sensor for Ca^{2+}-dependent inactivation of L-type calcium channels. *Neuron* **22,** 549–558 (1999).
72. Lee, S. R., Adams, P. J. & Yue, D. T. Large $Ca2^{+}$-dependent facilitation of Ca_v 2.1 channels revealed by Ca^{2+} photo-uncaging. *J. Physiol.* **593,** 2753–2778, doi: 10.1113/JP270091 (2015).
73. Sali, A. & Blundell, T. L. Comparative protein modelling by satisfaction of spatial restraints. *J. Mol. Biol.* **234,** 779–815, doi: 10.1006/jmbi.1993.1626 (1993).
74. Payandeh, J., Gamal El-Din, T. M., Scheuer, T., Zheng, N. & Catterall, W. A. Crystal structure of a voltage-gated sodium channel in two potentially inactivated states. *Nature* **486,** 135–139, doi: 10.1038/nature11077 (2012).
75. Li, R. A. *et al.* Clockwise domain arrangement of the sodium channel revealed by (mu)-conotoxin (GIIIA) docking orientation. *J. Biol. Chem.* **276,** 11072–11077, doi: 10.1074/jbc.M010862200 (2001).

Acknowledgements

We are grateful to Dr. Evan E. Eichler for investigating the previously unreported clinical phenotype of the proband and generously sharing relevant results with us. We thank Wanjun Yang for dedicated technical support and Ingie Hong for providing us with neuronal stimulus waveforms and experimental input. We also thank Gordon Tomaselli for providing valuable advice and discussions, and members of the Calcium Signals Lab for ongoing feedback. This work was supported by grants NIMH R01MH065531 and NHLBI 5R37HL076795 (D.T.Y.).

Author Contributions

W.B.L. contributed to all aspects of the experiments and data analysis. M.B.-J. assisted with the initial experimental design and homology modeling of the channel. W.B.L. and I.E.D wrote the manuscript with notes from D.T.Y. and input from all authors. D.T.Y. conceived the project and supervised the work.

Additional Information

Supplementary information accompanies this paper at http://www.nature.com/srep

Competing financial interests: The authors declare no competing financial interests.

How to cite this article: Limpitikul, W. B. *et al.* An autism-associated mutation in $Ca_V1.3$ channels has opposing effects on voltage- and Ca^{2+}-dependent regulation. *Sci. Rep.* **6**, 27235; doi: 10.1038/srep27235 (2016).